



## Validation study on a scaling law model of the DEM in industrial gas-solid flows

Yuki Mori <sup>a</sup>, Chuan-Yu Wu <sup>b</sup>, Mikio Sakai <sup>c,\*</sup>

<sup>a</sup> Department of Nuclear engineering and management, School of Engineering, The University of Tokyo, 7-3-1 Hongo, Bunkyo-ku, Tokyo 113-8656, Japan

<sup>b</sup> Department of Chemical and Process Engineering, University of Surrey, Guildford, Surrey GU2 7XH, UK

<sup>c</sup> Resilience Engineering Research Center, School of Engineering, The University of Tokyo, 7-3-1 Hongo, Bunkyo-ku, Tokyo 113-8656, Japan

### ARTICLE INFO

#### Article history:

Received 29 August 2018

Received in revised form 15 October 2018

Accepted 2 November 2018

Available online 03 November 2018

#### Keywords:

Discrete element method

DEM-CFD

Coarse grain model

Fluidized bed

Die filling

### ABSTRACT

Large-scale gas-solid flow systems, e.g., fluidized beds, cyclone separators and pneumatic conveyors, are often encountered in chemical engineering. Numerical modeling technologies are widely applied for design and understanding of complex phenomena in these gas-solid flow systems, for which the coupled model of the discrete element method (DEM) and computational fluid dynamics is generally employed. However, application of the numerical simulations for these systems is still limited because the number of the particles that can be modeled (about several hundreds of thousand) is quite small comparing with the immeasurable number of particles used in the industrial processes, and not sufficient to fully understand the complex behavior in these processes. The coarse graining DEM is then developed to provide an alternative approach for modeling the real industrial processes. Accuracy of the coarse graining DEM has been proven for simple systems so far. In the present study, applicability of the coarse graining DEM for complex shaped domains is explored, for which typical industrial processes, such as fluidization with inserted tubes, and powder flow into a confined space, are considered. In these calculations, signed distance functions (SDF) and immersed boundary method (IBM) are used to model an arbitrary shape wall boundary in a gas-solid flow. Both numerical modeling using the coarse graining DEM and experimental investigation are performed with a thorough comparison between the experimental and numerical results. It is demonstrated that the coarse graining DEM is capable of accurately modeling of industrial gas-solid two-phase systems. Besides, this numerical approach is shown to provide valuable information such as pressure profile during powder injection and interaction between bubbles and structures in a fluidized bed.

© 2018 Elsevier B.V. All rights reserved.

## 1. Introduction

Numerical simulations of gas-solid flows such as fluidization [1–9], pneumatic conveying [10], die filling [11–15] and cyclone separation [16,17] were extensively performed in chemical engineering. In these numerical simulations, the coupled discrete element method (DEM) [18] with computational fluid dynamics (CFD) was commonly employed. However, industrial applications of DEM-CFD method [1] are still limited because the number of the calculated particles is not sufficiently large comparing to the actual particle number used in the processes. The number of simulated particles is actually hundreds of thousand, although over billion particles are actually handled in the industrial processes. In order to overcome the limitation on the number of simulated particles, several scaling law models [6–10,19,20] were proposed such as a coarse graining DEM. In the coarse graining DEM, large-sized pseudo-particles were introduced to represent a group of the original particles. In such a way, the number of the simulated

particles could be reduced drastically. In our coarse graining DEM [6–10], the total energy was modeled to agree between the coarse grain particles and the group of original particles in binary collisions. Accuracy of the coarse graining DEM was demonstrated in simple rectangular or cylindrical systems so far. However, the coarse grain DEM has not been applied for a system with complex domains, although the geometry of most industrial systems is generally complex.

Recently the signed distance function (SDF) [21] was developed to model complex shaped boundaries in the DEM. Indeed, the SDF makes it easy to create an arbitrary shape boundary without any complex algorithm, which is achieved by defining the wall boundary with a scalar field composed of the distance between the particle surface and sign indicating inside or outside of the computation domain. Hence, the particle-to-wall interaction could be modeled without resorting to any complex algorithm. The robustness of the SDF in the DEM was proved for real industrial systems [22], such as a screw conveyor [21], a twin-screw kneader [23] and a ribbon mixer [24]. For modeling arbitrary shaped boundaries using the CFD, the immersed boundary method (IBM) [25–28] was introduced, in which an arbitrary shaped wall boundary could be modeled by simply evaluating the local volume

\* Corresponding author.

E-mail address: [mikio\\_sakai@n.t.u-tokyo.ac.jp](mailto:mikio_sakai@n.t.u-tokyo.ac.jp) (M. Sakai).

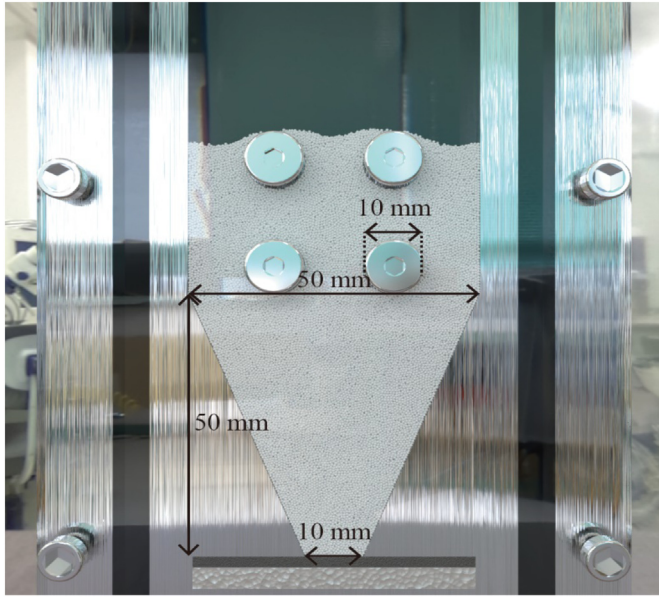


**Fig. 1.** Schematic diagram of the fluidized bed with inserted tubes.

**Table 1**  
Physical properties in a fluidized bed.

Gas phase	
Viscosity	$1.8 \times 10^{-5}$ Pa·s
Density	1.0 kg/m <sup>3</sup>
Solid phase	
Density	2500 kg/m <sup>3</sup>
Diameter	100 μm
Spring constant	50 N/m
Coefficient of restitution	0.9
Coefficient of friction	0.3

**Table 2**  
Validation conditions in a fluidized bed.

	Case 1-1	Case 1-2
Number of particles	250,000	
Coarse grain ratio	5.0	
Diameter of original particles	0.1 mm	
Diameter of calculated particles	0.5 mm	
Superficial velocity	0.2 m/s	0.3 m/s

fraction of a solid object. Recently, a density-scaled IBM [29] was also developed, where accuracy of the fluid flow was improved. A combination of the SDF and the IBM provides a simple but precise approach to model complex-shaped wall boundaries in fluid flow simulations. The DEM-CFD method incorporated with the SDF and the IBM was referred to as Advanced DEM-CFD method [12], for which its accuracy was validated for modeling die-filling processes with a small number of particles. However, the applicability of the Advanced DEM-CFD for large particle systems is still limited without the coarse grain model.

Therefore, in the current study, the capability of the Advanced DEM-CFD method is further enhanced with the implementation of the coarse graining DEM, in order to model large particle systems with arbitrary shaped boundaries. For the first time, an integrated DEM-CFD method with the coarse graining DEM, the SDF and the IBM is developed and its robustness is evaluated. Two case studies with the integrated DEM-CFD method are considered: fluidization with inserted tubes and powder flow into a confined space. Corresponding physical experiments are also performed in order to validate the integrated DEM-CFD method.

## 2. Numerical model

In the integrated DEM-CFD method, the solid phase is modeled using DEM, in which the coarse grain model is introduced. The gas phase is modeled by local volume average technique. The SDF and IBM are employed to model the wall boundaries for the solid and gas phases, respectively.

### 2.1. Solid phase modeling

The solid phase (i.e. particles) is analyzed using the coarse grain model. In the coarse grain model, a coarse grain particle represents a collection of original particles, for which the governing equations of solid phase, namely, translational and rotational motions of solid particles, are given as

$$m^{CGM} \frac{d\mathbf{v}^{CGM}}{dt} = \sum \mathbf{F}_C^{CGM} + \mathbf{F}_d^{CGM} - V_S^{CGM} \nabla p + m^{CGM} \mathbf{g} \quad (1)$$

and

$$I^{CGM} \frac{d\boldsymbol{\omega}^{CGM}}{dt} = \mathbf{T}^{CGM}, \quad (2)$$

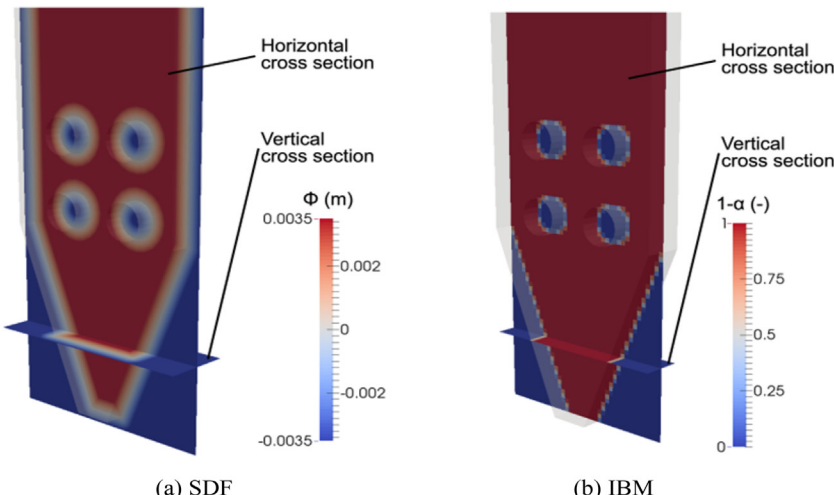


**Fig. 2.** SDF and IBM in the fluidized bed with inserted tubes.

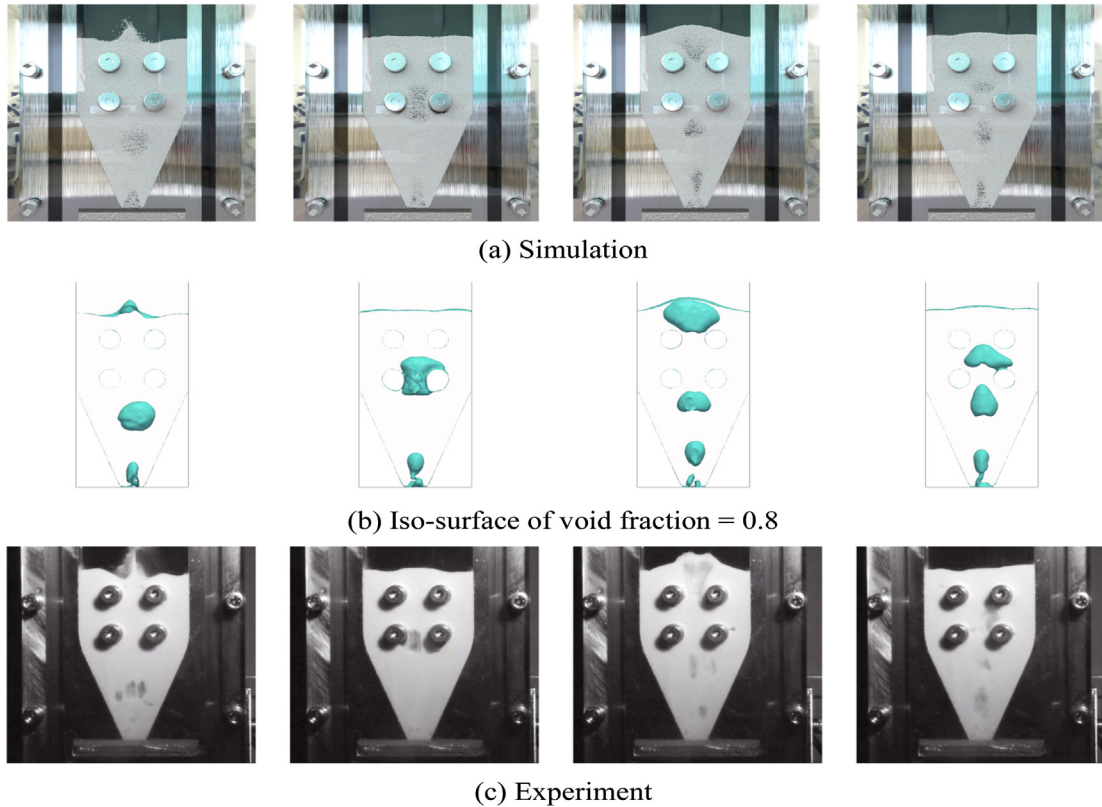


Fig. 3. Validation test results in Case 1-1.

where  $m$ ,  $\mathbf{v}$ ,  $t$ ,  $F_G$ ,  $\mathbf{F}_d$ ,  $V_S$ ,  $p$ ,  $\mathbf{g}$ ,  $I$ ,  $\omega$  and  $\mathbf{T}$  are, respectively, the particle mass, translational velocity of the particle, time, contact force, solid-fluid interaction force, particle volume, pressure, gravitational acceleration, momentum inertia, angular velocity of the particle, and torque. The superscript CGM refers a parameter of coarse grain particles.

The diameter of the coarse grain particles becomes  $l$  times larger than that of original particles, where  $l$  is the coarse grain ratio. Relationship of the original and coarse grain particle systems is given as follows

$$r^{CGM} = lr^0, \quad (3)$$

$$m^{CGM} = l^3 m^0, \quad (4)$$

$$V_S^{CGM} = l^3 V_S^0, \quad (5)$$

and

$$I^{CGM} = l^5 I^0, \quad (6)$$

where,  $r$  is the particle radius. Superscript  $O$  denotes a parameter of original particles.

The contact force acting on a coarse grain particle is modeled based on the conservation of kinetic energy between the coarse grain particles and the original particles. When two coarse grain particles collide, all the original particles assumed to make a binary collision in the coarse grain particles. The velocity of coarse grain particle is then modeled as the average velocity of the group of original particles. The contact force acting on a coarse grain particle consists of normal and tangential components, i.e.

$$\mathbf{F}_C^{CGM} = \mathbf{F}_{C_n}^{CGM} + \mathbf{F}_{C_t}^{CGM}. \quad (7)$$

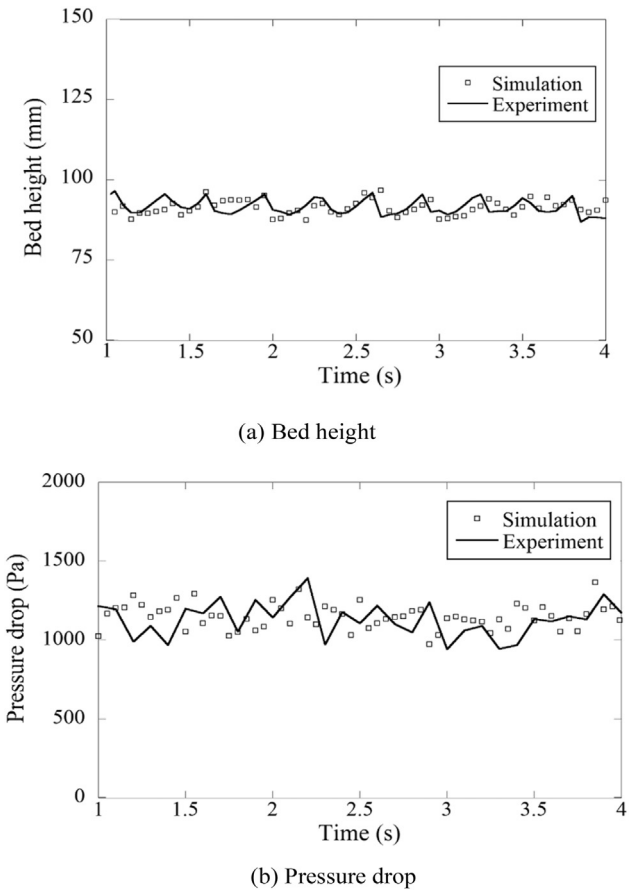


Fig. 4. Comparison of bed height and pressure drop between simulation and experiment in Case 1-1.

$\mathbf{F}_{C_n}^{CGM}$  and  $\mathbf{F}_{C_t}^{CGM}$  are given as

$$\mathbf{F}_{C_n}^{CGM} = l^3 \left( -k\delta_n^{CGM} - \eta\mathbf{v}_{r_n}^{CGM} \right) \quad (8)$$

and

$$\mathbf{F}_{C_t}^{CGM} = \begin{cases} l^3 \left( -k\delta_t^{CGM} - \eta\mathbf{v}_{r_t}^{CGM} \right) & |\mathbf{F}_{C_n}^{CGM}| < -\mu |\mathbf{F}_{C_n}^{CGM}| \\ -l^3 \mu |\mathbf{F}_{C_n}^{CGM}| \frac{\mathbf{v}_{r_t}^{CGM}}{|\mathbf{v}_{r_t}^{CGM}|} & |\mathbf{F}_{C_n}^{CGM}| \geq -\mu |\mathbf{F}_{C_n}^{CGM}| \end{cases} \quad (9)$$

where,  $k$ ,  $\delta$ ,  $\eta$ ,  $v_r$  and  $\mu$  are spring constant, displacement, the damping coefficient, relative velocity, and coefficient of friction, respectively. Subscript  $n$  and  $t$  represent the normal and tangential components, respectively. In the coarse graining DEM, original physical properties such as spring constant, coefficient of restitution and coefficient of restitution can be directly used, and hence total energy agrees between the original particle system and coarse graining particle one.

The drag force acting on a coarse grain particle is given by

$$\mathbf{F}_d^{CGM} = \frac{\beta V_S^{CGM}}{1-\epsilon} (\mathbf{u} - \mathbf{v}^{CGM}), \quad (10)$$

where,  $\beta$ ,  $\epsilon$  and  $\mathbf{u}$  are, respectively, the interphase momentum transfer coefficient, the void fraction and the fluid velocity.

It is clear that, in the coarse grain model, the solid phase can be analyzed using the physical properties of original particles. Readers are referred to references [8, 10] for more detailed discussion on the coarse graining DEM, such as algorithm, scheme and implementations.

## 2.2. Gas phase modeling

The modeling of the gas phase is the same as the conventional DEM-CFD method. The governing equations are Navier-Stokes and continuity equations, where the local volume average method [30] is employed. The governing equations are given as

$$\frac{\partial(\varepsilon\rho\mathbf{u})}{\partial t} + \nabla \cdot (\varepsilon\rho\mathbf{u}\mathbf{u}) = -\varepsilon\nabla p + \mathbf{F}_s + \nabla \cdot (\varepsilon\boldsymbol{\tau}) + \varepsilon\rho\mathbf{g}, \quad (11)$$

and

$$\frac{\partial\varepsilon}{\partial t} + \nabla \cdot (\varepsilon\mathbf{u}) = 0, \quad (12)$$

where,  $\rho$ ,  $\mathbf{F}_s$  and  $\boldsymbol{\tau}$  are the fluid density, the drag force acting on the fluid, and viscous tensor. The relationship between the drag forces  $\mathbf{F}_s$  and  $\mathbf{F}_d$  is determined by the Newton's third law of motion, i.e.

$$\mathbf{F}_s = -\frac{\sum \mathbf{F}_d^{CGM}}{V_{grid}}, \quad (13)$$

where  $V_{grid}$  is a volume of fluid grid. A combination of Ergun [31] and Wen-Yu [32] equations is commonly employed for the coefficient  $\beta$ , which is given as

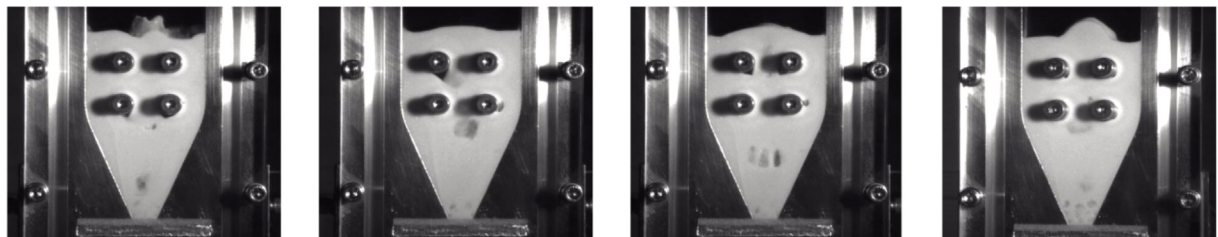
$$\beta = \begin{cases} 150 \frac{(1-\epsilon)^2 \mu}{\epsilon (2r^0)^2} + \frac{1.75(1-\epsilon)\rho}{2r^0} |\mathbf{u} - \mathbf{v}^{CGM}| & (\epsilon \leq 0.8) \\ \frac{3}{4} \frac{C_D(|\mathbf{u} - \mathbf{v}^{CGM}| \epsilon (1-\epsilon))}{2r^0} \epsilon^{-2.65} & (\epsilon > 0.8) \end{cases} \quad (14)$$



(a) Simulation

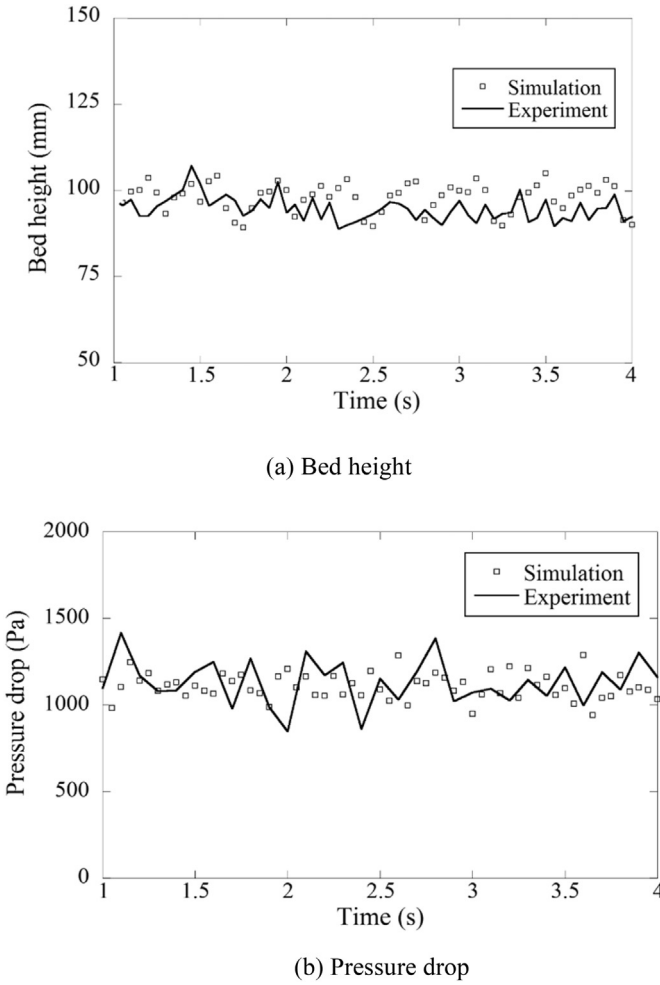


(b) Iso-surface of void fraction = 0.8



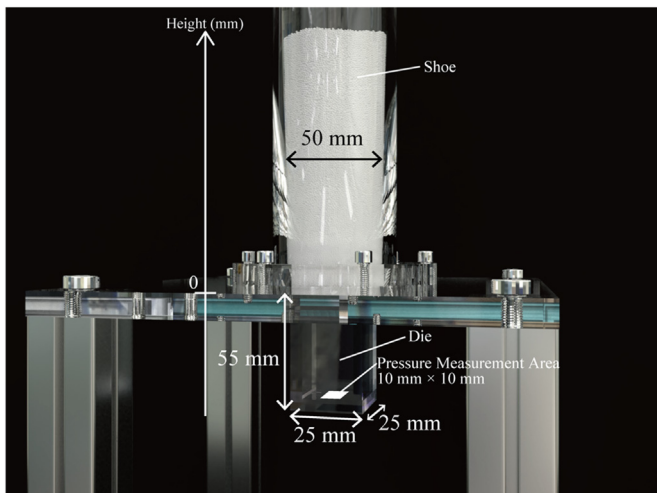
(c) Experiment

Fig. 5. Validation test results in Case 1-2.



**Fig. 6.** Comparison of bed height and pressure drop between simulation and experiment in Case 1-2.

$$C_D = \begin{cases} \frac{24(1 + 0.15Re^{0.687})}{Re} & (Re \leq 1000) \\ 0.44 & (Re > 1000) \end{cases} \quad (15)$$



**Fig. 7.** Geometrical configuration of a 3D stationary die-filling.

and

$$Re = \frac{|\mathbf{u} - \mathbf{v}^{CGM}| \rho \epsilon (2r^0)}{\mu} \quad (16)$$

where  $\mu$ ,  $C_D$  and  $Re$  are, respectively, the fluid viscosity, the drag coefficient and the Reynolds number.

### 2.3. Wall boundary modeling

Efficient treatment of arbitrary shaped walls is of great importance in modeling of complex industrial systems because the complex structures and geometrical boundaries are common. In this study, the wall boundaries for the solid and gas phases are modeled using the SDF [21] and the IBM [29], respectively. The combination of the SDF and the IBM makes it possible to model complex shaped boundaries easily and effectively in the DEM-CFD method. The most advantage of this combination is that the wall boundary can be created by a simple operation, specifically using the number of grids without tedious description of the geometrical shape. The details of wall boundary models for the DEM and CFD are discussed below.

#### 2.3.1. Wall boundary modeling in the DEM

In this study, the wall boundary modeling based on the SDF [21] was employed for the DEM. When the SDF is employed, wall boundary can be created by not mesh but scalar field. Reliability of the SDF is extensively validated in complex shape boundary systems [23,24,33–35], and accuracy of the SDF is shown to be equivalent to that of the mesh-based wall boundary [21]. The SDF is saved in spatial points with even interval in the calculation domain. The SDF is denoted as  $\phi(\mathbf{x})$ , and given as

$$\phi(\mathbf{x}) = s(\mathbf{x})d(\mathbf{x}) \quad (17)$$

where  $s(\mathbf{x})$  and  $d(\mathbf{x})$  are, respectively, the sign at a given point of  $\mathbf{x}$  and the distance between this point and the wall boundary.  $s(\mathbf{x})$  becomes positive when the points are inside of the calculational domain. The normal component of the particle-wall contact force  $\mathbf{n}_{p-w}$  and overlap  $\delta_{p-w_n}^{CGM}$  are derived as

$$\mathbf{n}_{p-w} = \frac{\nabla\phi}{|\nabla\phi|}, \quad (18)$$

and

$$\delta_{p-w_n}^{CGM} = (\phi - r^{CGM}) \mathbf{n}_{p-w} \quad (19)$$

From the gradient of kinetic energy, the contact force between the particle and the wall is given as

$$\mathbf{F}_{c_n}^{CGM} = l^3 \left( -k \delta_{p-w}^{CGM} |\nabla\phi| - \eta \mathbf{v}_{r_n}^{CGM} \right). \quad (20)$$

The tangential force is obtained in the same way as the particle-particle contact force.

#### 2.3.2. Wall boundary modeling in the CFD

The IBM can analyze the solid-fluid interaction with structured grids. In this method, the volume-weighted average velocity is used to analyze the interaction between the fluid and the solid object. The volume-weighted average velocity  $\mathbf{u}$  is calculated as

$$\mathbf{u} = (1 - \alpha) \mathbf{u}_{fluid} + \alpha \mathbf{u}_{wall} \quad (21)$$

where  $\alpha$ ,  $\mathbf{u}_{fluid}$  and  $\mathbf{u}_{wall}$  are the volume fraction of solid object, the fluid velocity, and the velocity of solid object, respectively. In Eq. (21),  $\alpha$  can be determined efficiently by counting the saved points of the SDF in a CFD grid. It should be noted that, in the IBM, this volume-weighted

**Table 3**

Physical properties in a die filling.

Gas phase		
Viscosity	$1.8 \times 10^{-5}$ Pa·s	
Density	1.0 kg/m <sup>3</sup>	
Solid phase		
Material name	CP-102®	NONPAREIL-108®
Density	1516 kg/m <sup>3</sup>	1483 kg/m <sup>3</sup>
Diameter	180 μm	100 μm
Spring constant	100 N/m	50 N/m
Coefficient of restitution	0.9	0.9
Coefficient of friction	0.3	0.3

**Table 4**

Validation conditions in a die filling.

	Case 2-1	Case 2-2	Case 3-1	Case 3-2
Particle material	CP-102®		NONPAREIL-108®	
Number of particles	120,941	362,821	88,898	266,693
Initial height	40 mm	120 mm	40 mm	120 mm
Coarse grain ratio	5.0		10	
Diameter of calculated particles	0.90 mm		1.0 mm	

velocity is used instead of fluid velocity, and all the calculated domain was solved as a fluid, even inside the solid object. In so doing, the correction term  $\mathbf{F}_{IB}$  must be considered, i.e.

$$\frac{\partial(\varepsilon p \mathbf{u})}{\partial t} + \nabla \cdot (\varepsilon p \mathbf{u} \mathbf{u}) = -\varepsilon \nabla p + \mathbf{f}_s + \nabla \cdot (\varepsilon \tau) + \varepsilon p \mathbf{g} + \mathbf{F}_{IB}. \quad (22)$$

This interaction force enforces the non-slip condition at the solid-fluid boundary. The force term  $\mathbf{F}_{IB}$  is given as

$$\mathbf{F}_{IB} = \frac{\alpha \varphi (\mathbf{u}_{wall} - \mathbf{u}_{fluid})}{\Delta t} \quad (23)$$

When the IBM is employed, the grid size should be finer than the object size, but it should be sufficiently larger than the particle size because of the use of the local volume average technique. Using the IBM, arbitrary shaped boundaries can be modeled in CFD, nevertheless rectangular grids are used. Essentially, effect of object shape on solid-fluid interaction can be modeled by  $\alpha$  in the IBM. In the previous study [27], fluid flowing in a complex shape domain was shown to be

accurately modeled by the IBM, where the  $\alpha$  was estimated based on the number of SDF pixels in a CFD grid.

In this study, a density scaling IBM was used, in which the density inside the object is scaled artificially. This is achieved through the introduction of the density scaling into the Poisson equation. When the Poisson equation is solved to obtain the fluid pressure, the scaled density  $\rho_{scale}$  is given by

$$\rho_{scale} = \begin{cases} \gamma \rho & (\phi < 0) \\ \rho & (\text{otherwise}) \end{cases} \quad (24)$$

where  $\gamma$  is the density scaling factor. The density scaling factor was 1000 in the present study. Consequently, the modified Poisson equation with the density scaling factor is expressed as

$$\nabla \cdot \left( \frac{\varepsilon^{n+1}}{\rho_{scale}} \nabla p^{n+1} \right) = \frac{1}{\Delta t} \left( \frac{\varepsilon^{n+1} - \varepsilon^n}{\Delta t} + \nabla \cdot \varepsilon^{n+1} \mathbf{u}^* \right) \quad (25)$$

where  $\mathbf{u}^*$  is the auxiliary fluid velocity. The role of  $\rho_{scale}$  is easy to understand when  $\gamma$  approaches  $\infty$ , indicating that all the grids inside a solid object ( $\phi < 0$ ) are then decoupled from the Poisson equation.

#### 2.4. Experimental validation

Two types of validation tests were performed: i) fluidization with inserted tubes and ii) powder flow into a confined space. Through these validation tests, the applicability of the integrated DEM-CFD method for these systems with arbitrary geometries is evaluated. These validation tests are discussed in detail in Section 3 and 4, respectively.

### 3. Validation test in a fluidized bed with inserted tubes

#### 3.1. Experimental set-up

A fluidized bed with 4 inserted tubes is considered. Fig. 1 shows a schematic diagram of this fluidized bed. The height, width and length were, respectively, 200 mm, 50 mm and 10 mm. Four tubes with a diameter of 10 mm were inserted in the fluidized bed. Table 1 illustrates the physical properties of the material used. Glass beads (UB-68 L, UNION Co. Ltd., Osaka, Japan) with an average diameter of approximately 100 μm were used in the experiments. The total amount of glass beads was set to 40.9 g. The inlet gas was air and its superficial velocity was set to 0.2 m/s (Case 1-1) and 0.3 m/s (Case 1-2) for two cases considered.

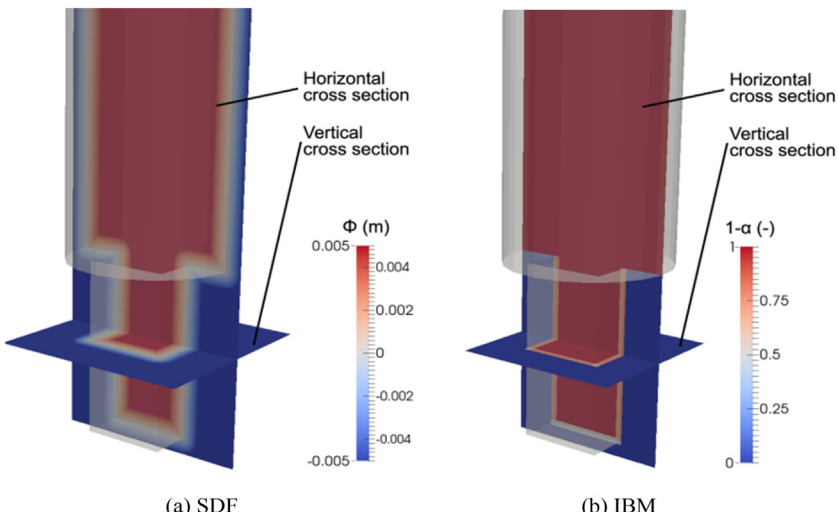
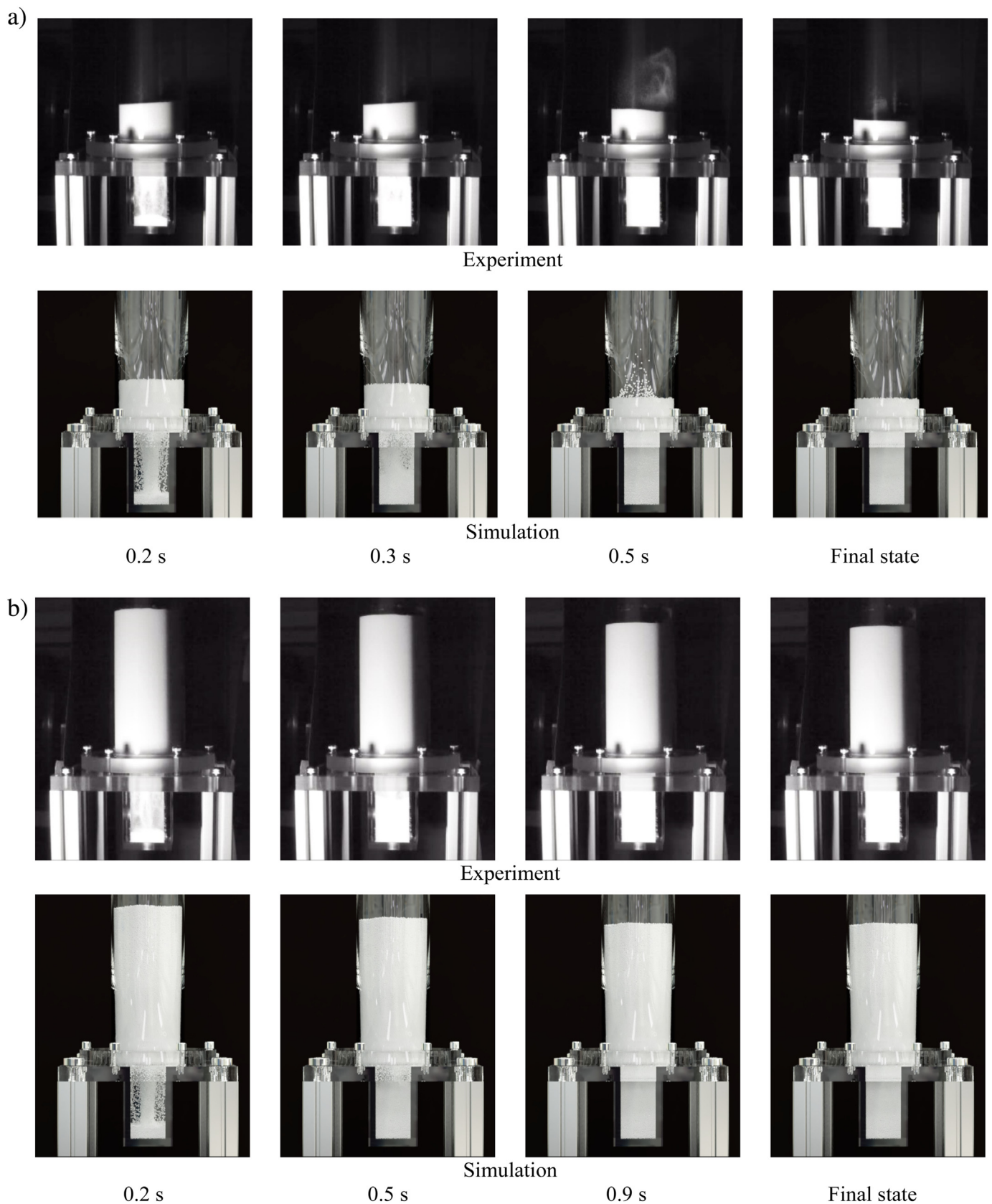
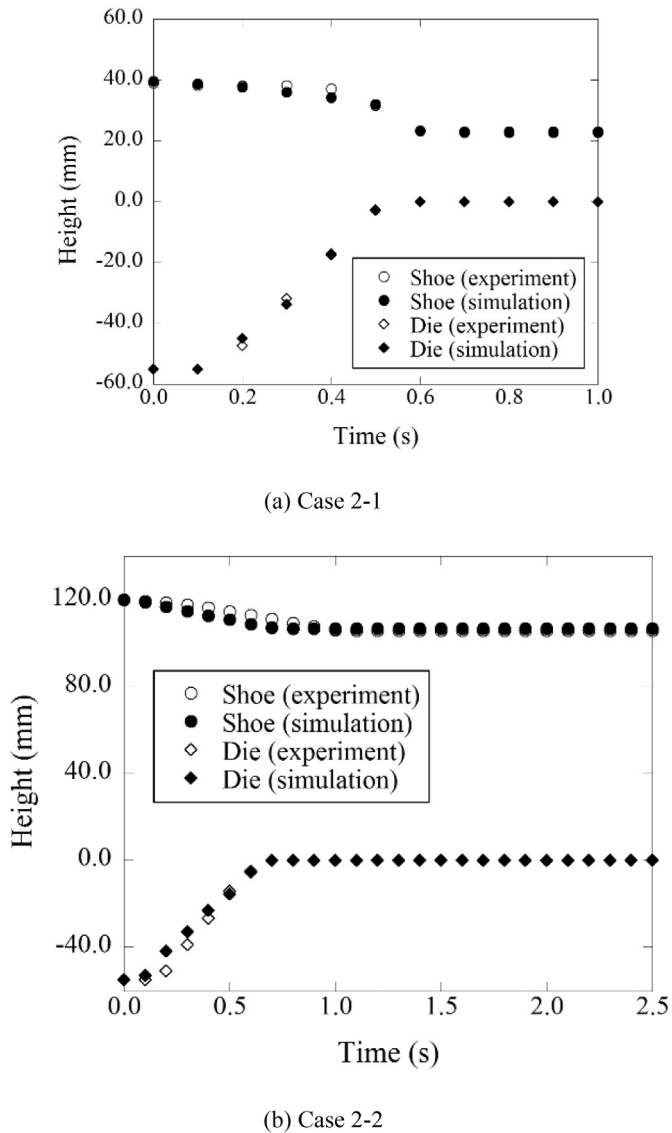


Fig. 8. SDF and IBM in the Stationary die-filling system.



**Fig. 9.** (a). Typical snapshots of validation test in Case 2-1. (b). Typical snapshots of validation test in Case 2-2.



**Fig. 10.** Comparison of bed height in the shoe and the die.

### 3.2. Simulations

In the simulations, the original particle diameter was set to 100  $\mu\text{m}$ , i.e. identical to that used in the experiment, and the coarse grain ratio was set to 5.0. The spring constant, the coefficient of friction and the

coefficient of restitution were set as 50 N/m, 0.3 and 0.9, respectively. **Table 2** designates the simulation conditions. The total number of simulated particles was 250,000, with the same total mass as that used in the experiment. The time step was set to  $1.0 \times 10^{-6}$  s. The CFD grid size was set to 1.25 mm in x, y and z directions. The wall boundaries were modeled by the SDF and the IBM in the DEM and the CFD, respectively, which are illustrated in vertical and horizontal cross sections in **Fig. 2**. In **Fig. 2a**, the blue and red regions represent, respectively, inside and outside of the computational domain in the DEM. Sign of the SDF became negative inside the object, and vice versa. **Fig. 2b** illustrates the local volume fraction of fluid phase ( $1-\alpha$ ), and blue area indicates inside of a solid in the CFD. The upward inlet gas velocity at the bed bottom was set as 0.2 m/s or 0.3 m/s for Case 1-1 and Case 1-2, respectively.

### 3.3. Results and discussion

For Case 1-1, where the superficial velocity was 0.2 m/s, typical snapshots in quasi-steady state for spatial location of the calculated particles, analyzed iso-surface of the void fraction being 0.8 and spatial location of solid particles in the experiment are shown in **Fig. 3**. In the quasi-steady state, splashes due to moving-up bubbles and fluctuation of the top of the powder bed were observed. The flow patterns of the solid particles obtained in the simulations and the experiment were in good agreement. As illustrated in **Fig. 3(b)**, the bubble behavior was clearly observed. The bubble size became larger as the bubble moved up the bed. Interaction between bubbles and inserted rods could be simulated by the integrated DEM-CFD method. Quantitative comparison was made in terms of the powder bed height and the pressure drop as shown in **Fig. 4**. The average bed heights obtained numerically and experimentally were, respectively, 91.4 mm and 91.7 mm, while the corresponding average pressure drops were measured to be, respectively, 1148 Pa and 1130 Pa. It is clear that the numerical results were quantitatively in good agreement with the experimental measurements. This is attributed to the agreement of total energy between the original and coarse grain particle systems, and besides the coarse grain ratio was given suitably.

For Case 1-2, where the superficial gas velocity was increased to 0.3 m/s, typical snapshots in the quasi-steady state are illustrated in **Fig. 5**. Splashes due to the bursting of bubbles and fluctuation of the powder bed could be observed, and similar powder flow patterns were obtained from the simulations and the experiments. Since the superficial velocity in Case 1-2 was higher than that in Case 1-1, the bubble size in Case 1-2 became larger than that in Case 1-1. In the same manner as Case 1-1, as the bubble went up the bed, bubble size became larger. Complex interaction between the bubbles and inserted rods could be observed in the simulation. Powder bed height and pressure drop were also obtained numerically and experimentally for quantitative comparison. As illustrated in **Fig. 6**, the average bed heights in the quasi-steady state obtained from the simulation and experiments were, respectively, 98.0 mm and 94.9 mm. The corresponding average pressure drops are 1108 Pa and 1131 Pa, respectively. It is clear that the integrated DEM-CFD method could accurately predict macroscopic phenomena such as the bed height and the pressure drop in complex gas-solid flow in fluidization, even with the coarse grain particles. Consequently, calculation results obtained from combination of the coarse graining DEM, SDF and IBM was shown to be accurate, though the calculation algorithm was very simple.

## 4. Validation test in powder flow into a confined vessel

### 4.1. Experimental set-up

Powder flow into a confined space in air, simulating die filling with a stationary shoe, was also considered to further evaluate the integrated

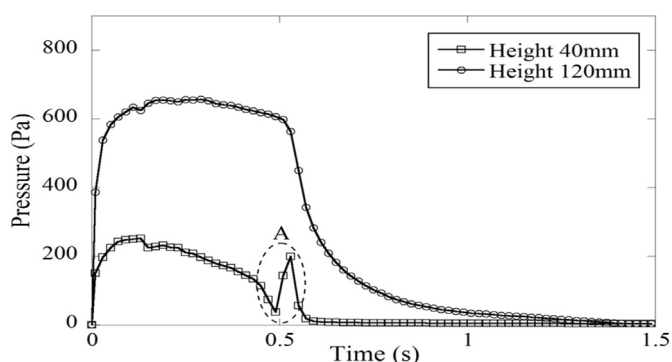


**Fig. 11.** Transient change of pressure in the die.

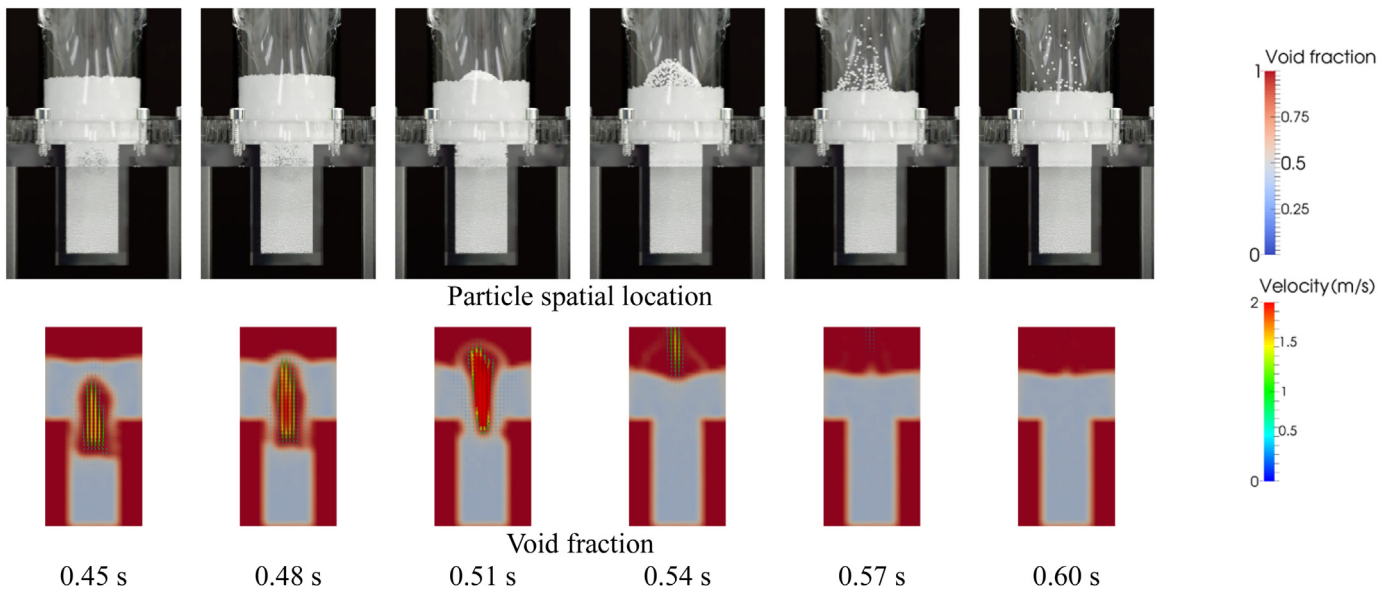


**Fig. 12.** Particle spatial location and void fraction in the die around 0.5 s (corresponding to B in Fig. 12).

DEM-CFD method. Fig. 7 shows the geometrical configuration of the model system. The height, width and length of the die were, respectively, 25 mm, 25 mm and 50 mm. The powder was initially loaded in a cylindrical vessel above the die. Two powders were used in the present study, i.e. CP-102® (Asahi Kasei, Tokyo, Japan) and NONPAREIL-108® (FREUND CORPORATION, Tokyo, Japan). Table 3 lists the physical properties of these two powders. The average diameter of CP-102® particle and NONPAREIL-108® particle was approximately 180  $\mu\text{m}$  and 100  $\mu\text{m}$ , respectively. Two different initial powder bed heights, namely 40 mm and 120 mm, were considered for each powder.

#### 4.2. Numerical simulations

In this study, a mono-dispersed system was assumed and the diameter of the original particles of CP-102® and NONPAREIL-108® was 180  $\mu\text{m}$  and 100  $\mu\text{m}$ , respectively. The spring constant, coefficient of friction and coefficient of restitution were set as 50 N/m, 0.3 and 0.9, respectively. Table 4 shows the simulation conditions. The number of calculated particles was 120,941, 362,821, 88,898 and 266,693, respectively, in Case 2-1, Case 2-2, Case 3-1 and Case 3-2, where the height corresponded to that in the experiment. The particle density of CP-102® particle and NONPAREIL-108® particle was estimated to be, respectively, 1516 kg/m<sup>3</sup> and 1483 kg/m<sup>3</sup> from the powder bed volume and the powder mass, and the coarse grain ratio was set to 5.0 and 10.0 in Case 2 and Case 3, respectively. The time step was set to  $1.0 \times 10^{-6}$  s. The CFD grid size was 1.25 mm in x, y and z directions. The wall boundary was modeled using the SDF and the IBM, respectively, in the DEM and the CFD. Fig. 8 illustrates the SDF and the IBM in the vertical and horizontal cross sections. In Fig. 8a, blue and red regions were, respectively, inside and outside of the computational domain. Again, the SDF became negative inside the object. In Fig. 8b, the blue region indicates inside of the object, namely, local volume fraction of fluid became <1.0. The simulated particles were randomly packed in the cylinder when the initial particle locations were provided.

#### 4.3. Results and discussion

For CP-102, i.e. the particle with a diameter of 180  $\mu\text{m}$ , two cases were considered: Case 2-1 and Case 2-2, where the bed

height was 40 mm in Case 2-1 and 120 mm in Case 2-2. Fig. 9 shows typical powder flow patterns obtained from simulations and experiments for Case 2-1 and Case 2-2. It is clear that the overall powder flow patterns obtained from the simulations and experiments were similar. In addition, it is interesting to observe that splash was occurred once at a time instant around 0.5 s in Case 2-1, but no splash was observed in Case 2-2. Quantitative comparison of the bed height was made in shoe and die regions for Case 2-1 and Case 2-2. Fig. 10 shows the transient change of bed height in the shoe and the die, where connecting point of cylinder and die was zero in height. In both cases, the evolutions of bed heights obtained from the calculation and experiments were in excellent agreement. For Case 2-1, the bed height in the shoe was gradually reduced initially, then drops suddenly around 0.5 s, before reaching a constant value. This is because the sudden drop of powder bed height was induced by the splash. In the die, the powder bed monotonically increased until the die was fully filled by the powder. For Case 2-2, until the die was fully filled by powder, the bed height monotonically decreased in the shoe, but monotonically increased in the die.

In the simulation, the air pressure change at the bottom of the die was also examined and shown in Fig. 11 for both Case 2-1 and Case 2-2. It can be seen that, for Case 2-1 (powder height was 40 mm), the fluid pressure increased immediately as the powder started to flow into the die, and a sharp peak was observed around 0.5 s (marked A with circle in Fig. 11), finally the pressure reduced to zero. During the time period from 0.2 s to 0.4 s, air gradually permeated from the powder bed, which caused the pressure to reduce gradually. The sudden pressure change was induced due to the bubble splash. In order to discuss the sudden pressure drop in Case 2-1, a detailed examination of the particle spatial distribution and the void fraction during the period from 0.45 s to 0.60 s is presented in Fig. 12. When the powder flowed into the die, a bubble was generated in the bulk powder in the die, and moved upward. It then burst and a splash occurred around 0.5 s, the powder rapidly moved and filled the region occupied by the bubble. This led to the pressure peak around 0.5 s. However, the pressure change for Case 2-2 was different. In Case 2-2, the pressure first increased, and finally decreased without any peak. The pressure increase was mainly induced as a result of pressurization of air in the die as its volume reduced when the powder flowed into the die. The pressure

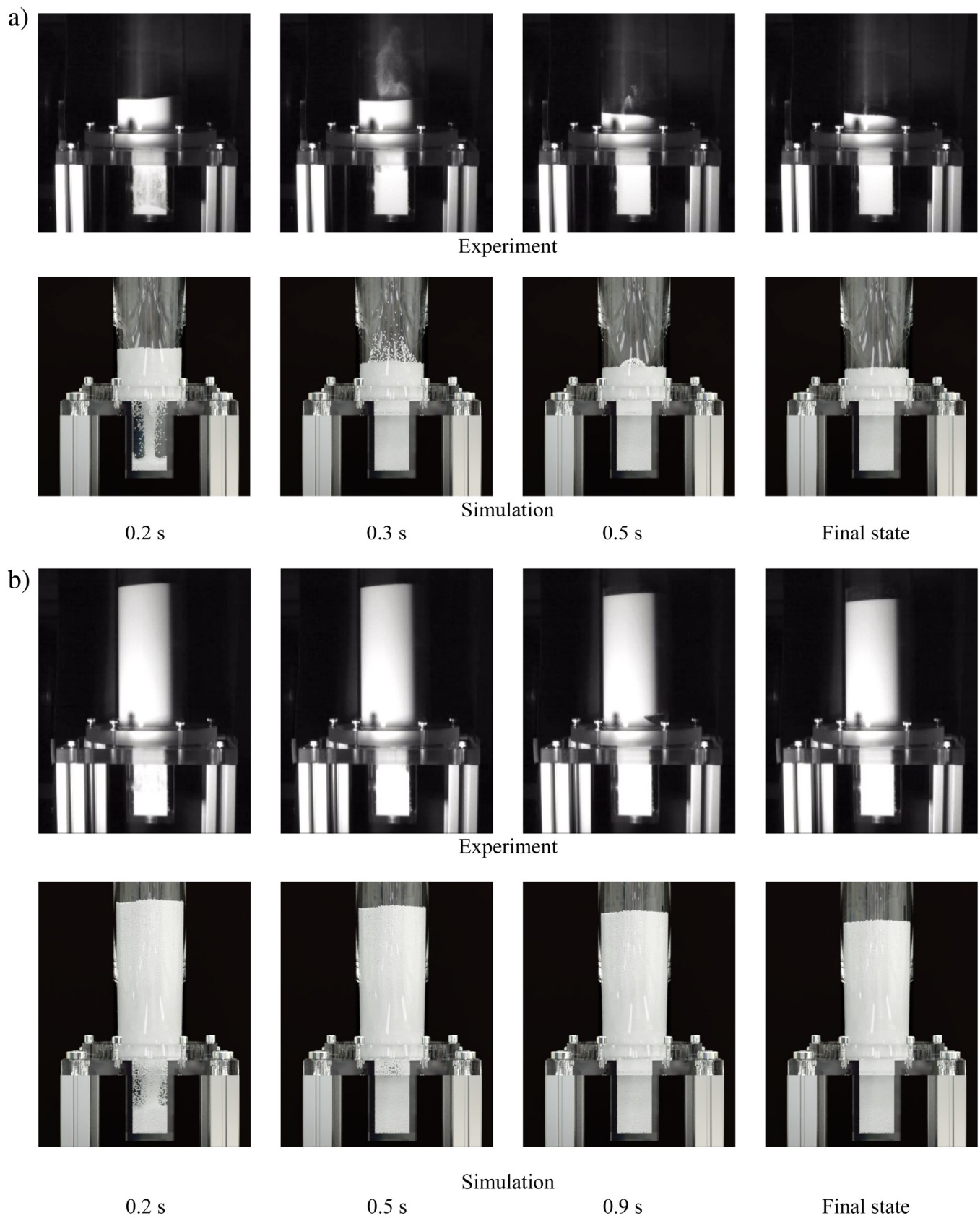
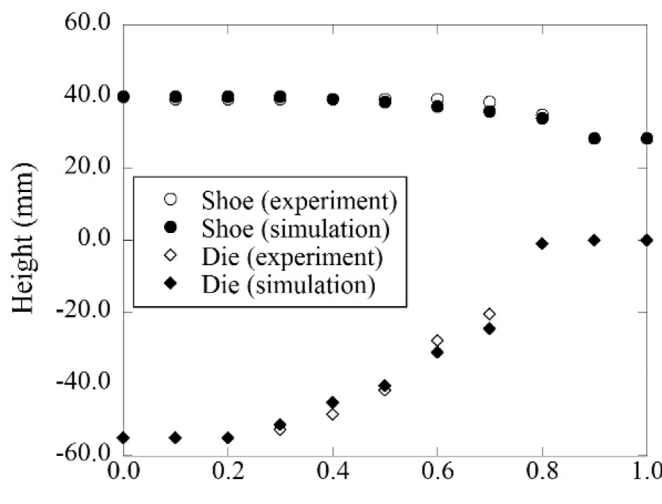
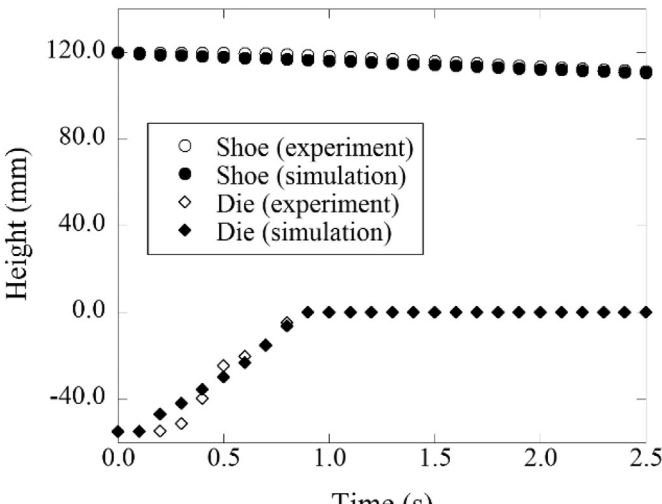


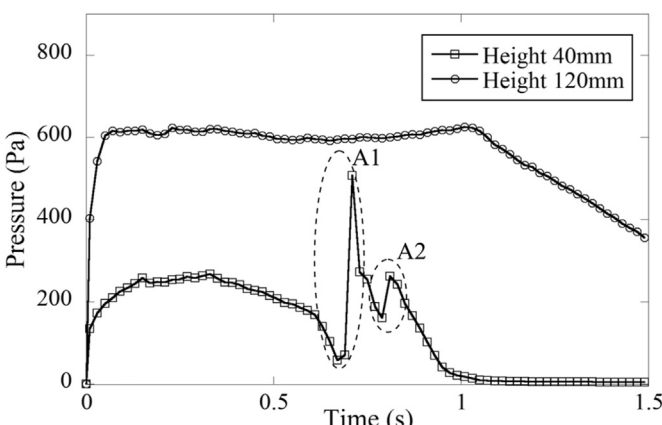
**Fig. 13.** (a). Comparison of typical snapshot in case 2-1 between simulation and experiment. (b). Comparison of typical snapshot in case 2-2 between simulation and experiment.



(a) Case 3-1



(b) Case 3-2

**Fig. 14.** Comparison of bed height in shoe and die between simulation and experiment.**Fig. 15.** Transient change of pressure in the die (Case 3).

decreased at the late stage of the process occurred primarily due to air permeation from the bulk powder.

Similar to CP-102, two cases (Case 3-1, or Case 3-2) were considered for NONPAREIL. The bed height was 40 mm in Case 3-1 and 120 mm in Case 3-2. Fig. 13 shows the powder flow patterns obtained numerically and experimentally. It is clear that the overall powder flow pattern was in qualitative agreement between computations and experiments. It is interesting to observe that splash occurred twice around 0.7 s and 0.9 s in Case 3-1, but no splash took place in Case 3-2. Fig. 14 shows the corresponding evolutions of the bed height in the shoe and the die. It could be seen that good agreement between the computations and experiments was quantitatively obtained in terms of the bed heights. For Case 3-1, the bed height was gradually reduced, then reasonably changed with different rate around 0.7 s and 0.8 s, finally became static state. These height changes were induced by the occurrence of splashes. In the die, the powder bed monotonically increased until the die was fully filled. However, for Case 3-2, the bed height in the shoe monotonically decreased, while it monotonically increased in the die until the die was full.

In the simulations, the change in air pressure at the bottom of the die was examined. Fig. 15 shows the transient pressure change in Case 3-1 and Case 3-2. In Case 3-1, the air pressure increased as soon as the powder started to flow into the die, but rarely changed in the time period from 0.2 s to 0.6 s. Thereafter, it decreased rapidly and two sharp peaks were observed during around 0.7 s and 0.8 s (marked A1 and A2 in Fig. 15). Finally, the pressure reduced to almost zero. The sudden pressure change and the two peaks were induced by the bubble splash. However, in Case 3-2, the pressure increased initially to reach a plateau that was maintained through the powder flow process, before started to reduce to zero at the end. In order to understand the sudden pressure change in Case 3-1, the particle spatial distribution and the void fraction in the time period from 0.60 s to 0.87 s were examined as shown in Fig. 16. When the powder flowed into the die, a long bubble was formed in the bulk powder in the die. When the first bubble burst (i.e. the occurrence of splash) at a time instant of around 0.7 s, the pressure was reduced sharply. After the first splash took place, the powder rapidly flowed in and broke the long bubble, then a small bubble was generated. This small bubble rose gradually to the surface of the powder bed until it burst to generate the second splash, at which the second pressure peak was induced. This demonstrates that the integrated DEM-CFD enables a detailed investigation on complex gas-solid flows.

## 5. Conclusions

An integrated DEM-CFD method combining the coarse graining DEM for modeling large particle systems with the SDF and the IBM for modeling arbitrary boundaries was developed in this study. Its capability and accuracy were demonstrated with two case studies: i) fluidization with inserted tubes and ii) powder flow into a confined space. Experiments were also performed to validate the integrated DEM-CFD method. The main advantages of the integrated DEM-CFD method were i) the ability to model large particle systems of industrial relevance, for which the incorporation of the coarse grain DEM dramatically reduced the simulated particle numbers; and ii) easy but accurate modeling of complex boundaries, which was achieved with the combination of the SDF (for solid phase) and the IBM (for fluid phase). Comparison between the experimental measurement and the modeling results illustrated that the integrated DEM-CFD method could accurately reproduce the experimental results, specifically, macroscopic behavior of solid phase (e.g., spatial particle location and splash) and gas phase (e.g., pressure drop). Furthermore, the integrated DEM-CFD method was shown to provide valuable data such as interaction between bubbles and tubes in a fluidized bed, and pressure profile in powder injection into a confined vessel.

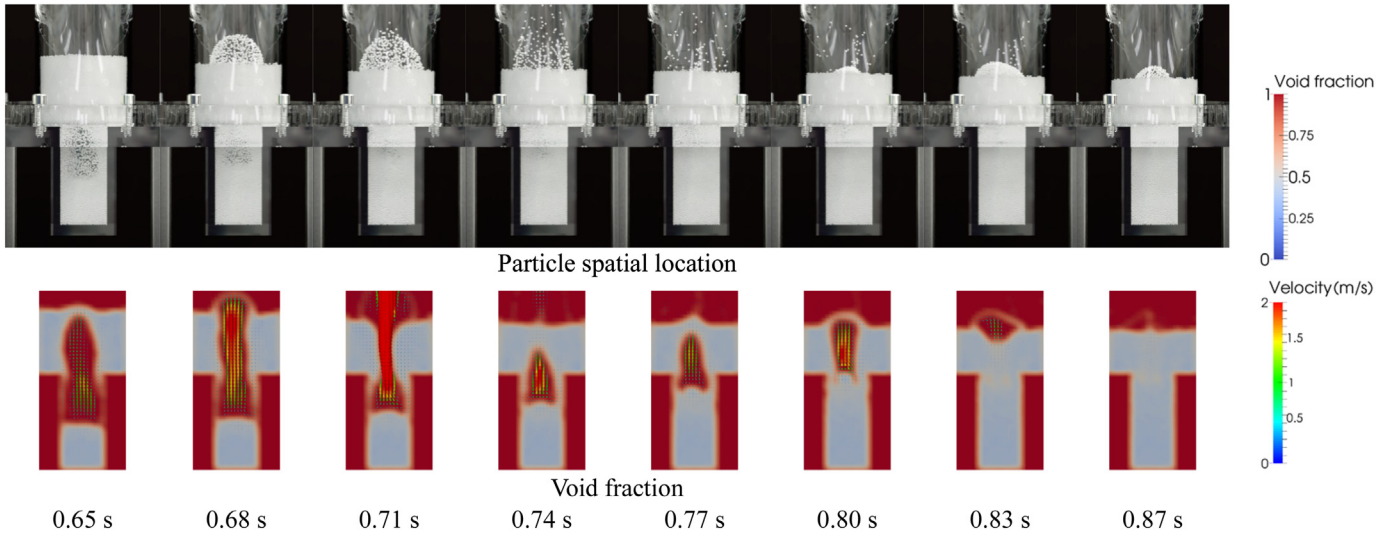


**Fig. 16.** Particle spatial location and void fraction in the die around 0.5 s (corresponding to A1 and A2 in Fig. 15).

## Acknowledgements

This study was financially supported by JSPS KAKENHI Grant Numbers 17KK0110. The samples of glass beads (UB-68L), CP-102® particle and NONPAREIL-108® were provided by UNION Co. Ltd., Asahi Kasei and FREUND CORPORATION, respectively.

## References

- [1] Y. Tsuji, T. Kawaguchi, T. Tanaka, Discrete particle simulation of two-dimensional fluidized bed, *Powder Technol.* 77 (1993) 79–87.
- [2] C.M. Boyce, A. Ozel, J. Kolehmainen, S. Sundaresan, Analysis of the effect of small amounts of liquid on gas-solid fluidization using CFD-DEM simulations, *AIChE J.* 63 (2017) 5290–5302.
- [3] J. Gan, Z. Zhou, A. Yu, CFD-DEM modeling of gas fluidization of fine ellipsoidal particles, *AIChE J.* 62 (2015) 62–77.
- [4] Q.F. Hou, S.B. Kuang, A.B. Yu, A DEM-based approach for analyzing energy transitions in granular and particle-fluid flows, *Chem. Eng. Sci.* 161 (2017) 67–79.
- [5] S. Yang, K. Luo, J. Fan, K. Cen, Particle-scale investigation of the solid dispersion and residence properties in a 3-D spout-fluid bed, *AIChE J.* 60 (2014) 2732–3090.
- [6] M. Sakai, Y. Yamada, Y. Shigeto, K. Shibata, V.M. Kawasaki, S. Koshizuka, Large-scale discrete element modeling in a fluidized bed, *Int. J. Numer. Meth. Fluids* 64 (2010) 1319–1335.
- [7] M. Sakai, H. Takahashi, C.C. Pain, J.-P. Latham, J. Xiang, Study on a large-scale discrete element model for fine particles in a fluidized bed, *Adv. Powder Technol.* 23 (2012) 673–681.
- [8] M. Sakai, M. Abe, Y. Shigeto, S. Mizutani, H. Takahashi, A. Viré, J.R. Percival, J. Xiang, C.C. Pain, Verification and validation of a coarse grain model of the DEM in a bubbling fluidized bed, *Chem. Eng. J.* 244 (2014) 33–43.
- [9] K. Takabatake, Y. Mori, J.G. Khinast, M. Sakai, Numerical investigation of a coarse-grain discrete element method in solid mixing in a spouted bed, *Chem. Eng. J.* 346 (2018) 416–426.
- [10] M. Sakai, S. Koshizuka, Large-scale discrete element modeling in pneumatic conveying, *Chem. Eng. Sci.* 64 (2009) 533–539.
- [11] Y. Tsuzawa, Y. Shigeto, C. Tokoro, M. Sakai, Numerical simulation of industrial die filling using the discrete element method, *Chem. Eng. Sci.* 138 (2015) 791–809.
- [12] H. Yao, Y. Mori, K. Takabatake, X. Sun, M. Sakai, Numerical investigation on the influence of air flow in a die filling process, *J. Taiwan Inst. Chem. Eng.* 90 (2018) 9–17.
- [13] Y. Guo, C.-Y. Wu, K.D. Kafui, C. Thornton, 3D DEM/CFD analysis of size-induced segregation during die filling, *Powder Technol.* 206 (2011) 177–188.
- [14] Y. Guo, K.D. Kafui, C.Y. Wu, C. Thornton, J.P.K. Seville, A coupled DEM/CFD analysis of the effect of air on powder flow during die filling, *AIChE J.* 55 (2009) 49–62.
- [15] C.Y. Wu, DEM simulations of die filling during pharmaceutical tabletting, *Particuology* 6 (2008) 412–418.
- [16] K.W. Chu, J. Chena, B. Wang, A.B. Yu, A. Vince, G.D. Barnett, P.J. Barnett, Understand solids loading effects in a dense medium cyclone: Effect of particle size by a CFD-DEM method, *Powder Technol.* 320 (2017) 594–609.
- [17] K.W. Chu, B. Wang, D.L. Xu, Y.X. Chen, A.B. Yu, CFD – DEM simulation of the gas – solid flow in a cyclone separator, *Chem. Eng. Sci.* 66 (2011) 834–847.
- [18] P.A. Cundall, O.D.L. Strack, A discrete numerical model for granular assemblies, *Geotechnique* 29 (1979) 47–65.
- [19] K. Chu, J. Chen, A. Yu, Applicability of a coarse-grained CFD-DEM model on dense medium cyclone, *Miner. Eng.* 90 (2016) 43–54.
- [20] L. Lu, J. Xu, W. Ge, Y. Yue, X. Liu, J. Li, EMMS-based discrete particle method (EMMS-DPM) for simulation of gas-solid flows, *Chem. Eng. Sci.* 120 (2014) 67–87.
- [21] Y. Shigeto, M. Sakai, Arbitrary-shaped wall boundary modeling based on signed distance functions for granular flow simulations, *Chem. Eng. J.* 231 (2013) 464–476.
- [22] M. Sakai, How should the discrete element method be applied in industrial systems?: a review, *KONA Powder Part. J.* 33 (2016) 169–178.
- [23] M. Sakai, Y. Shigeto, G. Basinskas, A. Hosokawa, M. Fuji, Discrete element simulation for the evaluation of solid mixing in an industrial blender, *Chem. Eng. J.* 279 (2015) 821–839.
- [24] G. Basinskas, M. Sakai, Numerical study of the mixing efficiency of a ribbon mixer using the discrete element method, *Powder Technol.* 287 (2016) 380–394.
- [25] S. Das, S. Sneijders, N.G. Deen, J.A.M. Kuipers, Drag and heat transfer closures for realistic numerically generated random open-cell solid foams using an immersed boundary method, *Chem. Eng. Sci.* 183 (2018) 260–274.
- [26] H.V. Patel, S. Das, J.A.M. Kuipers, J.T. Padding, E.A.J.F. Peters, A coupled Volume of Fluid and Immersed Boundary Method for simulating 3D multiphase flows with contact line dynamics in complex geometries, *Chem. Eng. Sci.* 166 (2017) 28–41.
- [27] X. Sun, M. Sakai, Numerical simulation of two-phase flows in complex geometries by using the volume-of-fluid /immersed-boundary method, *Chem. Eng. Sci.* 139 (2016) 221–240.
- [28] H. Udon, M. Sakai, A numerical study on dynamic inertial focusing of microparticles in a confined flow, *Granul. Matter* 19 (2017) 79.
- [29] X. Sun, M. Sakai, Immersed boundary method with artificial density in pressure equation for modeling flows confined by wall boundaries, *J. Chem. Eng. Jpn.* 50 (2017) 161–169.
- [30] T.B. Anderson, R. Jackson, Fluid mechanical description of fluidized beds. Equations of motion, *Ind. Eng. Chem. Fund.* 6 (1967) 527–539.
- [31] S. Ergun, Fluid flow through packed columns, *Chem. Eng. Prog.* 48 (1952) 89–94.
- [32] C.Y. Wen, Y.H. Yu, Mechanics of fluidization, *Chem. Eng. Progr. Symp. Ser.* 62 (1966) 100–111.
- [33] G. Basinskas, M. Sakai, Numerical study of the mixing efficiency of a batch mixer using the discrete element method, *Powder Technol.* 301 (2016) 815–829.
- [34] X. Sun, M. Sakai, M.-T. Sakai, Y. Yamada, A Lagrangian-Lagrangian coupled method for three-dimensional solid-liquid flows involving free surfaces in a rotating cylindrical tank, *Chem. Eng. J.* 246 (2014) 122–141.
- [35] Y. Yamada, M. Sakai, Lagrangian-Lagrangian simulations of solid-liquid flows in a bead mill, *Powder Technol.* 239 (2013) 105–114.